2013

Automated cell-specific laser detection and ablation of neural circuits in neonatal brain tissue

Xueying Wang
William & Mary

John A. Hayes
William & Mary

Maria Cristina D. Picardo
William & Mary, mrdegu@wm.edu

Christopher A. Del Negro
William & Mary, cadeln@wm.edu

John A. Hayes
William & Mary

Recommended Citation

Guinamard, R., Simard, C., & Del Negro, C. (2013). Flufenamic acid as an ion channel modulator. Pharmacology & therapeutics, 138(2), 272-284.

JPn Neuroscience

The Journal of Physiology

J Physiol 591.10 (2013) pp 2393–2401

TECHNIQUES FOR PHYSIOLOGY

Automated cell-specific laser detection and ablation of neural circuits in neonatal brain tissue

Xueying Wang[1], John A. Hayes[1,2], Maria Cristina D. Picardo[1] and Christopher A. Del Negro[1]

[1] *Department of Applied Science, McGlothlin-Street Hall, The College of William & Mary, Williamsburg, VA 23187-8795, USA*
[2] *Department of Biology, Integrated Science Center, The College of William & Mary, Williamsburg, VA 23187-8795, USA*

Key points

- We developed an automated system that detects neurons belonging to specific populations *in vitro* or *in situ*, maps their physical locations in three-dimensional tissue specimens and then laser ablates the cell 'targets' one at a time, in sequence, while monitoring neural population activity electrophysiologically.
- Two-photon Ca^{2+} imaging and image processing routines detect and validate target neurons based on rhythmic Ca^{2+} fluorescence activity patterns.
- Visible-wavelength confocal imaging and image processing routines detect and validate target neurons that express genetically encoded fluorescent proteins.
- High-intensity two-photon spot scanning vaporizes target neurons with specificity while minimizing damage to neighbouring tissue.
- Physiological monitoring of network function is performed before, during and after the cell-specific laser ablations to measure the effects on network functionality in real time.

Abstract A key feature of neurodegenerative disease is the pathological loss of neurons that participate in generating behaviour. To investigate network properties of neural circuits and provide a complementary tool to study neurodegeneration *in vitro* or *in situ*, we developed an automated cell-specific laser detection and ablation system. The instrument consists of a two-photon and visible-wavelength confocal imaging setup, controlled by executive software, that identifies neurons in preparations based on genetically encoded fluorescent proteins or Ca^{2+} imaging, and then sequentially ablates cell targets while monitoring network function concurrently. Pathological changes in network function can be directly attributed to ablated cells, which are logged in real time. Here, we investigated brainstem respiratory circuits to demonstrate single-cell precision in ablation during physiological network activity, but the technique could be applied to interrogate network properties in neural systems that retain network functionality in reduced preparations *in vitro* or *in situ*.

(Received 25 October 2012; accepted after revision 21 February 2013; first published online 25 February 2013)
Corresponding author C. A. Del Negro: Department of Applied Science, McGlothlin-Street Hall, Room 318, The College of William & Mary, Williamsburg, VA 23187-8795, USA. Email: cadeln@wm.edu

Abbreviations 3D, three-dimensional; preBötC, pre-Bötzinger complex; ROI, region of interest; XII, hypoglossal.

Introduction

Lesion tools allow neuroscientists to examine the cellular bases for behaviours and to model neuropathology (e.g. Liu & Fetcho, 1999; McKay *et al.* 2005; Eklof-Ljunggren *et al.* 2012). Ideally, one removes particular neurons from a circuit via ablation, and then measures the effect on network function. However, gaining new knowledge from this type of experimental paradigm depends on three key factors: (1) how selectively a class of neurons can be

X. Wang and J. A. Hayes contributed equally to this work.

DOI: 10.1113/jphysiol.2012.247338

distinguished from its neighbours and thus targeted for ablation, (2) how accurately the neurons of interest can be ablated while minimizing damage to surrounding tissues and (3) how sensitively lesion effects on network output can be monitored.

Here we demonstrate an automated cell-specific laser detection and ablation system. It is designed for use in reduced preparations that retain behaviourally relevant activity *in vitro* or *in situ*. A visible-wavelength laser and an adjustable long-wavelength laser are used to detect specific neurons based on genetically encoded fluorescent reporter proteins or functional criteria such as rhythmic Ca^{2+} activity, respectively. The three-dimensional (3D) coordinates of cell somata are stored as a list of targets in memory. Cell targets are drawn from the list randomly, or in any user-defined sequence, and then laser-ablated one at a time, cumulatively, while monitoring network function via electrophysiology. Subsequent perturbations of network output can be directly attributed to the lesioned neurons because the tally and map of ablated neurons are tracked in real time. Custom software controls all the hardware and carries out the protocol. Two-photon excitation provides confocal specificity and control of each lesion in three dimensions, while causing minimal extraneous damage to surrounding tissue.

We recently used rhythmic Ca^{2+} activity to detect and ablate rhythm-generating neurons of the respiratory central pattern generator, but the details of the methods have not been previously described (Hayes *et al.* 2012). Here we document the methodology, including the algorithms for detection and targeting, and demonstrate its applicability for detecting and ablating neurons based on fluorescent reporter protein expression in addition to Ca^{2+} activity.

Methods

Ethical approval

The Institutional Animal Care and Use Committee at The College of William & Mary, which ensures compliance with United States federal regulations concerning care and use of vertebrate animals in research, approved the following protocols. The specific regulations are codified in the Department of Agriculture, 9th code of federal regulations (parts 1 and 2), Public Health Service 99-158.

Neonatal mouse slice preparations

We used C57BL/6 (wild type, WT) and transgenic mice that express *Cre* recombinase fused to the tamoxifen-sensitive oestrogen receptor in neurons that express the transcription factor *Dbx1* ($Dbx1^{+/CreERT2}$) (Hirata *et al.* 2009). $Dbx1^{+/CreERT2}$ mice were coupled with *floxed* reporter mice that express the red fluorescent protein variant tdTomato in a *Cre*-dependent manner ($Rosa26^{tdTomato}$, Jax No. 007905) (Madisen *et al.* 2010). Thus, we obtained mice in which *Dbx1*-derived ($Dbx1^{+}$) neurons can be identified by red fluorescence in the soma and dendrites. The $Dbx1^{+/CreERT2}$ strain was bred in-house using a CD-1 background. The $Rosa26^{tdTomato}$ strain was maintained as a homozygous line with C57BL/6J background. We verified animal genotype via PCR using primers specific for *Cre* and tandem dimer red fluorescent protein (Transnetyx, Cordova, TN, USA). We also used $Dbx1^{+/LacZ}$ mice on a C57BL/6J background (Pierani *et al.* 2001) and identified heterozygous mutants using fluorescein-di-β-D-galactopyranoside, which is cleaved by the *lacZ* gene product, β-galactosidase, to activate its fluorescence (Gray *et al.* 2010). A total of 109 WT mice, 21 $Dbx1^{+/CreERT2}$;$Rosa26^{tdTomato}$ mice and four $Dbx1^{+/LacZ}$ mice were used in these studies.

Neonatal mice aged postnatal days 0–3 (P0–3) were killed following 4 min of immersion in crushed ice until there was no longer a pinch response from the animals (in compliance with the 2011 guidelines of the Animal Research Advisory Committee, Office of Animal Care and Use, National Institutes of Health, Bethesda, MD, USA). This method renders the animals insentient to the same degree as would occur with gaseous anaesthetics (Danneman & Mandrell, 1997; Fox *et al.* 2007) and facilitates the rapid isolation of the intact brainstem and spinal cord, which would otherwise be damaged if cervical dislocation were used to kill the animals. After the animals were anaesthetized and removed from the ice, two transections were performed at bregma and the thorax. The neuraxis, from the pons to the lower thoracic spinal cord, was then rapidly removed (~90 s) and subsequently dissected in a dish filled with artificial cerebrospinal fluid containing (in mM): 124 NaCl, 3 KCl, 1.5 $CaCl_2$, 1 $MgSO_4$, 25 $NaHCO_3$, 0.5 NaH_2PO_4, and 30 D-glucose, equilibrated with 95% O_2 and 5% CO_2 (pH 7.4). The neuraxis was isolated and pinned onto a paraffin-coated paddle, with its rostral side up and ventral surface facing out. The paddle was fixed into the vice of a vibrating microtome for sectioning in the transverse plane. We cut 400- to 500-μm-thick slices from the medulla that retain the pre-Bötzinger complex (preBötC) as well as hypoglossal (XII) motoneurons and premotor neurons with respiratory motor function.

Fluorescent labelling of Dbx1^{+} neurons

We crossed $Dbx1^{+/CreERT2}$ mice with $Rosa26^{tdTomato}$ *Cre*-dependent reporter mice to obtain $Dbx1^{+/CreERT2}$; $Rosa26^{tdTomato}$ pups. Tamoxifen administration to pregnant female mice on the tenth day after the plug date produced fluorescent $Dbx1^{+}$ neurons in ~50%

of the offspring. Using epifluorescence microscopy with a band-pass excitation filter (546–558 nm), a dichroic mirror (560 nm) and a band-pass barrier filter (575–640 nm), *Dbx1*$^{+}$ neurons could be visualized in the preBötC and contiguous regions of the dorsomedial medulla. Slices from *Dbx1*$^{+/Lacz}$ mice were incubated in artificial cerebrospinal fluid with 1.5 mg mL^{-1} of fluorescein-di-β-D-galactopyranoside for 30 min at 37°C to activate fluorescein.

Loading Ca^{2+}-sensitive fluorescent dye

Slices were loaded with the calcium-sensitive dye Quest Fluo-8 AM (AAT Bioquest, Sunnyvale, CA, USA) for fluorescent Ca^{2+} imaging of rhythmically active preBötC respiratory neurons. The slices were submerged in a loading solution in 1.5 ml centrifuge tubes for 1.5–2 h in the dark at 37°C. Loading solution consisted of 90 μl of 9 mM K^+ artificial cerebrospinal fluid, 10 μl D-mannitol stock solution (1 M) and 5 μl of Fluo-8 stock solution (50 μg Fluo-8 dissolved in 60 or 30 μl Pluronic F-127 20% solution in dimethyl sulfoxide) for a final Fluo-8 concentration of 32 or 64 μM.

After incubation in Fluo-8 AM loading solution, slices were mounted in a recording chamber and perfused with artificial cerebrospinal fluid at 27°C at 4 ml min^{-1}. The external potassium concentration ($[K^+]_o$) was raised to 9 mM and inspiratory motor output was recorded from XII nerve roots. Typically, 5 μM picrotoxin and 5 μM strychnine were added to the artificial cerebrospinal fluid to block chloride-mediated inhibitory transmission (disinhibition).

Imaging

We used a fixed-stage upright laser-scanning confocal microscope (LSM 510; Carl Zeiss Inc., Thornwood, NY, USA) equipped with visible-wavelength lasers and a tunable (710–920 nm) mode-locked Ti:sapphire laser (Mai Tai Rad X; Spectra Physics, Irvine, CA, USA). The Ti:sapphire laser generated pulses of <100 fs duration at 80 MHz for a wavelength of 800 nm. The average power of the pulsed laser was ~1 W at emission and measured ~36 mW through the objective at the specimen plane. All experiments used a 20×/1.0 numerical aperture (NA) water-immersion objective. The LSM 510 scan head contained three internal descanned detectors and two external non-descanned detectors used to collect fluorescent emissions. The recording chamber was secured on a robotic *xy* translation stage (Siskiyou Corp., Grants Pass, OR, USA), which moves the imaging plane between bilaterally distributed regions of the preBötC. The robotics were manually controlled at the start of the experiments, and then computer-controlled during the automated phases of the experiments.

Electrophysiology

Inspiratory motor rhythms were recorded from the XII nerve roots using suction electrodes and a differential amplifier. XII output is full-wave rectified and smoothed for display. XII measurements were normalized according to the average magnitude recorded during a steady-state control period prior to laser ablation. Whole-cell recordings employed an EPC-10 amplifier (HEKA Electronic, Bellmore, NY, USA). Patch solution contained (in mM): 140 potassium gluconate, 10 NaCl, 0.5 $CaCl_2$, 10 Hepes, 1 EGTA, 2 Mg-ATP and 0.3 Na_3-GTP (pH 7.3). We added 50 μM Alexa 568 hydrazide (Invitrogen, Carlsbad, CA, USA) for fluorescent identification of the recorded neurons. All electrophysiology data were filtered at 1 kHz and digitally acquired at 10 kHz using a 16-bit analog/digital converter (ADInstruments, Colorado Springs, CO, USA).

Ablator executive software

We wrote a suite of Python-language scripts that controlled all operations of the lesioning experiments including microscopy, motorized *xy* stage translation, online analysis and target detection, target selection, as well as laser ablation using the Ti:sapphire laser. We named this software Ablator, which is modular and can potentially control additional microscopes, robotic stages and other devices. Python is a general public licence-compatible open source programming language and features relatively simple syntax that facilitates cross-platform applicability and modularity. Ablator is available from http://sourceforge.net/projects/ablator/ and a detailed description of its functionality is provided in the following text and figures, as well as the Supplementary Methods.

Results

The instrument includes a master computer that controls a Ti:sapphire long-wavelength laser, a laser scanning microscope with visible-wavelength lasers and non-descanned detectors, as well as a customized robotic *xy* translation stage with specimen chamber. Another computer, time-synced to the master, monitors network activity via electrophysiology (Fig. 1*A*). The software package dubbed Ablator automates the experiments, which consist of three phases. The *initialization phase* defines the domain of the target area. Next, the *detection phase* employs two-photon or confocal microscopy with image processing to map cell populations in three dimensions and arrive at a final target list. Finally, the *ablation phase* selects the order and then sequentially destroys (or attempts to destroy) each entry in the target list until all the targets are exhausted. Physiological monitoring takes place continuously during the detection and ablation phases (Fig. 1*B*).

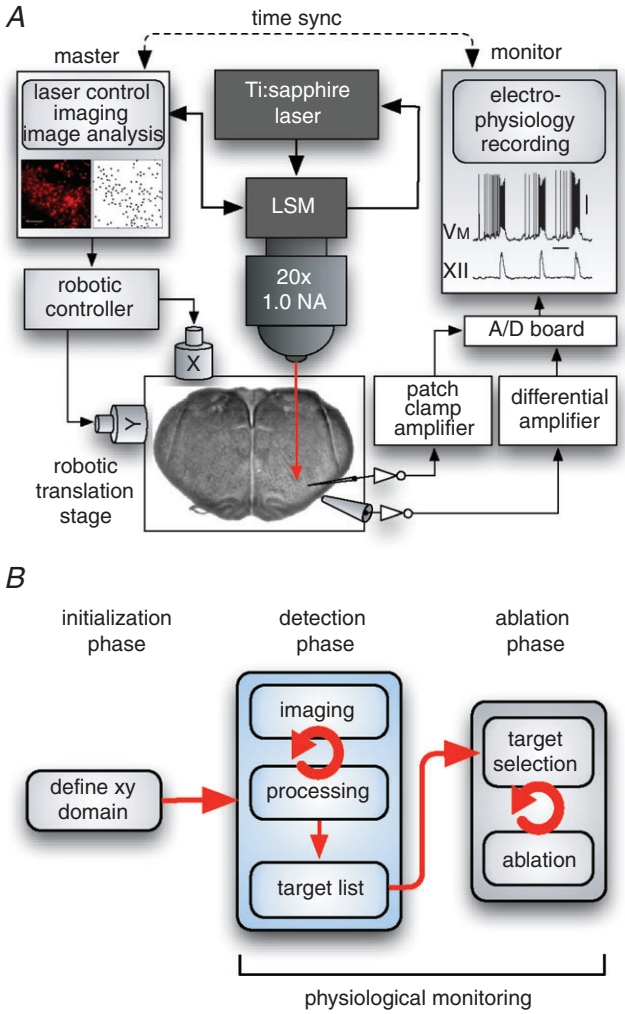

Figure 1. Cartoon of the hardware setup and executive software flow
A, the master computer (left) controls the Ti:sapphire laser as well as the laser scanning microscope (LSM) and robotic *xy* translation stage. The master also runs Ablator executive software to implement the protocols. The inset in the master computer panel represents image acquisition and analysis (scale bar = 100 μm). The robotic translation stage holds the specimen chamber where the inset image shows a brainstem slice preparation containing the hypothesized inspiratory centre pre-Bötzinger complex (preBötC). The monitoring computer (right) continuously performs extracellular suction electrode and/or patch-clamp recordings, which are standard tools to measure respiratory rhythm generation *in vitro*. The inset images reflect typical voltage trajectories for a preBötC neuron (V_M) and integrated hypoglossal (XII) nerve root (arbitrary units) during spontaneous breathing-related activity *in vitro*. Calibration bars = 20 mV (applies to V_M trace) and 1 s (applies to both V_M and XII traces). Amplifiers and the analog-to-digital (A/D) converter are shown in the schematic, too. Master and monitor computers are time synchronized. *B*, the basic three-phase protocol: initialization, detection and ablation. Each phase is described in the main text as well as Supplementary Methods. Essential information obtained during each phase of the experiment is passed (rightward) to the subsequent phase. Circular arrows indicate iterative steps in the detection and ablation phases. Physiological monitoring takes place continuously during the detection and ablation phases.

During the *initialization phase*, the experimenter controls the robotic *xy* translation stage and manoeuvres the specimen so that the region of interest (ROI) occupies the centre of the field of view. Ablator can accommodate a single uniform domain or a broader domain that consists of *n* isolated parts. Here we utilize a bilaterally distributed nucleus, the respiratory rhythmogenic preBötC of the ventral medulla, which retains the ability to generate breathing-related rhythms in transverse slice preparations (Smith *et al.* 1991; Feldman *et al.* 2013). This rhythmic slice is experimentally advantageous because the key rhythmogenic population in the preBötC can be exposed at the slice surface (Ruangkittisakul *et al.* 2006, 2011) for laser detection and subsequent ablation, while continuously monitoring respiratory motor output (Hayes *et al.* 2012). The user also defines the *z*-axis range, which depends on opacity of the tissue, the laser power and the emission properties of the fluorophore. Figure 2*A* illustrates a 400-μm-thick slice in which green-shaded regions indicate the *xy* domain containing the hot spot of rhythmic activity in the preBötC and a *z*-axis depth of 80 μm, which is typical for experiments that employ Ca^{2+} indicator dye in the preBötC (Ruangkittisakul *et al.* 2009; Hayes *et al.* 2012). The slice also retains oligosynaptic premotor circuits and XII motor neurons (Koizumi *et al.* 2008; Volgin *et al.* 2008). Respiratory motor output is measured via the XII cranial nerve rootlets (Fig. 2*A*). The *xy* domain is stored in memory so that the robotics can position the specimen appropriately during the detection and ablation phases.

The general strategy for target detection is to acquire and analyse images of the *xy* domain, including any and all sub-regions, at focal planes separated by 10 μm increments in the *z*-axis (e.g. Fig. 2*A*, centre). For Ca^{2+} imaging experiments, the system acquires time-series images. The stack is projected into one plane by calculating the standard deviation of the fluorescence intensity at each pixel through the stack (Fig. 2B_a). ROIs with large fluorescence changes stand out (e.g. 47, 83, 106, 115, 116, Fig. 2B_a), which is used to produce a mask of potential targets. Ablator finds local maxima via an iterative threshold-crossing routine and defines them as ROIs (Fig. 2B_b). Each ROI is then further analysed based on fluorescence changes from the original time series (Fig. 2C_{a-e}). To find preBötC neurons, Ablator applies Fourier analysis to search for significant power in the range 0.15–0.5 Hz (Fig. 2D_{a-e}), which is typical for respiratory rhythms *in vitro* (Smith *et al.* 1990, 1991; Ruangkittisakul *et al.* 2006, 2007; Feldman *et al.* 2013). If peak power falls in this range, then the final step evaluates the amplitude of fluorescence changes to ensure the oscillation is a robust one (Fig. 2E_{a-e}). Passing both the frequency and the amplitude tests, the ROI is accepted as a bona fide respiratory neuron. Whole-cell recordings suggest

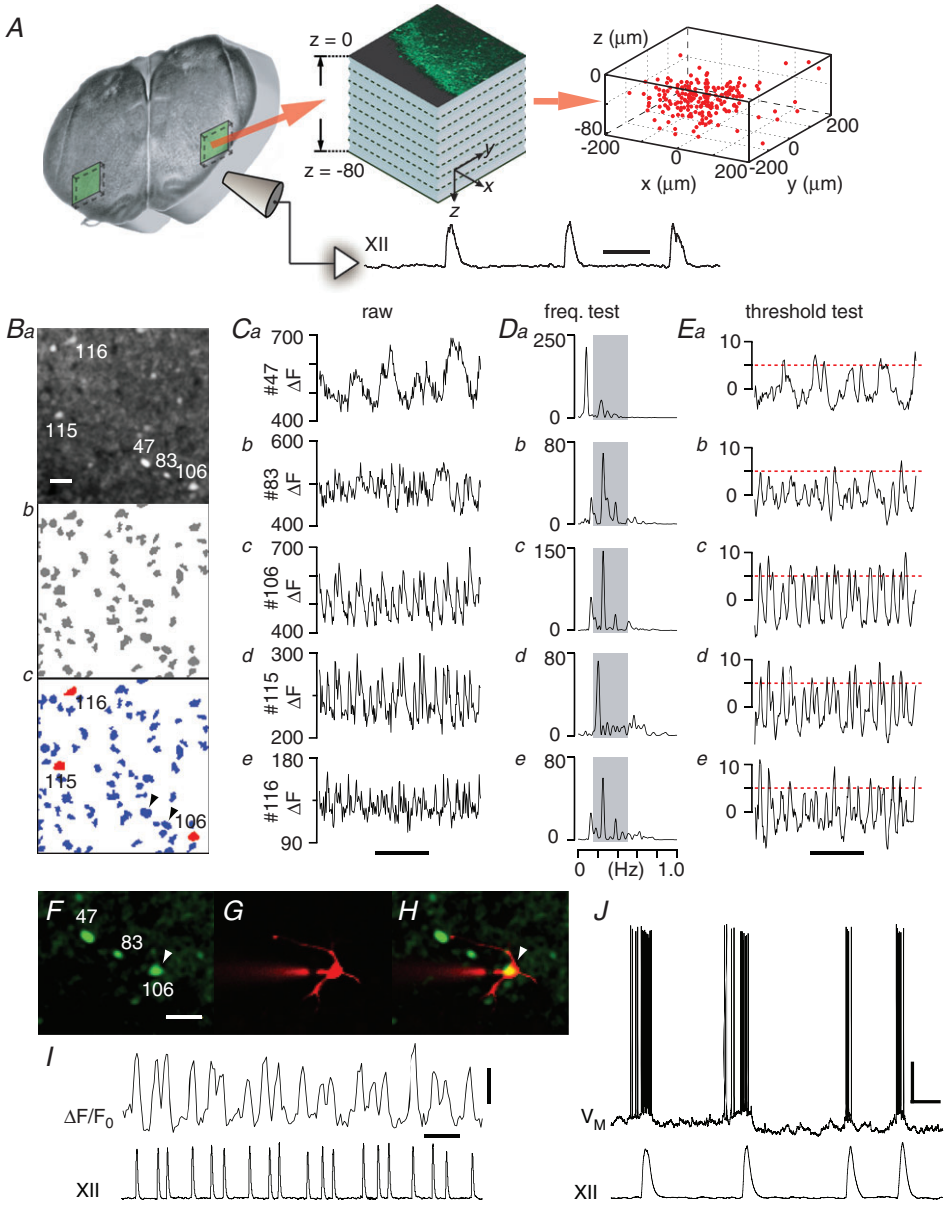

Figure 2. Automated cell target detection
A, slice preparation with spontaneous breathing-related motor output from the XII nerve (scale bar = 1 s). Green boxes demarcate the bilateral *xy* domain of the preBötC. Image stacks (middle) show 1 min acquisitions using Ca^{2+} indicator dye over the right preBötC. Each time series is repeated in 10 μm increments from the surface of the tissue to a final depth of 80 μm. The 3D map (right) shows the position of all validated cell targets (red) for the right preBötC. *B–E*, detecting cell targets via Ca^{2+} imaging. B_{a-c}, analysed image B_a shows the standard deviation (SD) of fluorescence changes (ΔF) for a 1 min Ca^{2+} imaging time series (scale bar = 40 μm). B_b, the mask of all potential targets from B_a; unevaluated ROIs are grey. B_c, the mask of validated (red) and rejected (blue) targets. C_{a-e}, raw ΔF activity is displayed for ROIs 47, 83, 106, 115 and 116 from B_a (scale bar = 20 s). D_{a-e}, the frequency test analyses power spectra computed from the time series in C_{a-e}, showing peak power as a function of characteristic frequency. The frequency band for respiratory rhythm *in vitro* (0.15–0.5 Hz) is shown in grey. E_{a-e}, the threshold test counts the peaks in the normalized ΔF time series that cross a user-defined level (dashed red line) (scale bar = 20 s). ROIs 106, 115 and 116 are valid targets because each crosses the threshold five or more times per minute. ROI 47 shows a large amplitude ΔF signal (C_a) with five threshold crossings (E_a), but its dominant frequency is <0.15 Hz so it is rejected. ROI 83 is rhythmically active in the expected frequency range (D_b) but fails the threshold test and thus is deemed too weak, and is rejected. *F*, SD image showing Ca^{2+} fluorescence with superimposed ROI labels (scale bar = 40 μm). *G*, the same neuron as in *F* filled with Alexa 568 through the patch pipette. *H*, merged image from *F* and *G*. *I*, $\Delta F/F_0$ from ROI 106 displayed with XII output (vertical scale 10% $\Delta F/F_0$, time scale 5 s). *J*, whole-cell recording with XII output (voltage scale 20 mV, time scale 1 s).

that automatically detected targets are robust respiratory neurons (Fig. 2*F–J*, $n = 5$).

Cells that express genetically encoded reporters (e.g. green fluorescent protein, yellow fluorescent protein (YFP), tdTomato) can also be automatically detected. Ablator acquires a higher-resolution image using a visible-wavelength laser and then calls the iterative threshold-crossing routine described above to find ROIs that represent all potential targets for the focal plane. A second stage of processing assigns a circularity score (C) to differentiate somata from neuropil or detritus. A C value approaching 0 indicates an increasingly elongated polygon; $C \sim 1$ indicates a perfect circle. If C falls below a user-specified cut-off, then the ROI is rejected. The circularity test distinguishes cell bodies from auto-fluorescent debris (Fig. 3A_{a-b}) and isolated segments of dendrites whose somata are detected in an adjacent plane and retained as a valid target (Fig. 3B_{a-b}, C_{a-b}, C_a', C_b'). A priority rule applied in the final stage eliminates redundant targets from adjacent planes. If two or more overlaying ROIs pass the circularity test, then the ROI from the earliest acquisition is retained and all others are rejected (Fig. 3C_b, C_b'; Supplementary Fig. 2).

Every ROI in the *xy* domain, throughout the *z*-axis, is analysed and the final target list is passed to the *ablation phase*, which begins as individual targets are drawn from the 3D volume (e.g. Fig. 2*A*). Selection is random by default. When the domain consists of non-contiguous sub-regions, a specified number of targets may be selected within a sub-domain before moving to another. Commonly, left–right alternation applies to preparations that preserve bilateral symmetry. The Ti:sapphire laser, tuned to 800 nm, is focused on one target. Maximum intensity scanning over a 110 μm^2 spot centred on the ROI is performed while acquiring an image with a 560–615 nm band-pass filter. Confirmation of ablation is obtained by applying a threshold-crossing algorithm to analyse the image in this range of wavelengths, which detects presumed water vapour in the cell cavity while excluding green emissions of Ca^{2+} indicator dyes or YFP as well as infrared reflections of the long-wavelength laser (Fig. 4*A*). Ablated cell targets vanish from the fluorescence images, providing an intuitive form of confirmation (Fig. 4B_{a-b}). Differential interference contrast imaging shows that in successful lesions, a pockmark replaces the original cell image (Fig. 4*C*, D_c). The cavity resulting from the lesion is limited to the borders of the cell and occupies less than 10 μm in the *z*-axis, demonstrating that the volume of damage is limited to the target ROI (Fig. 4D_{a-e}). Following lesion confirmation, Ablator chooses a new target and

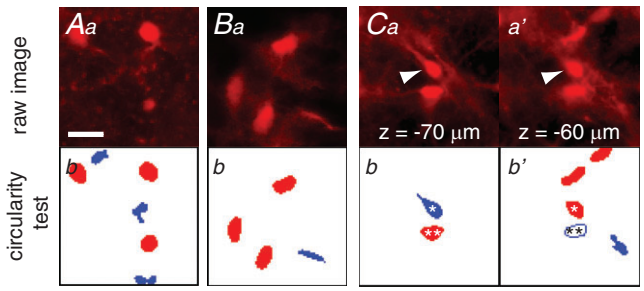

Figure 3. Detecting cell targets via fluorescent reporters
A_a, B_a, C_a and C_a', preBötC neurons from *Dbx1*^{CreERT2}; *Rosa26*^{tdTomato} mice, in which *Dbx1*-derived (*Dbx1*$^+$) neurons express tdTomato. Scale bar in A_a is 20 μm and applies to all panels. A_b, B_b, C_b and C_b', mask ROIs obtained by analysing the corresponding images above. Red ROIs are deemed valid targets by the circularity test; blue ROIs are rejected. Circularity analyses differentiate somata from auto-fluorescent detritus (A_a, A_b) as well as isolated pieces of dendrites (B_a, B_b). Non-somatic autofluorescence and isolated parts of dendrite are not valid targets, and thus are rejected. Circularity analysis furthermore rejects ROIs that include the soma plus an adjacent dendritic segment. A contiguous soma-dendrite ROI (C_a, C_b blue ROI *) is rejected in the –70 μm focal plane, but the same cell is validated by circularity analysis at –60 μm (C_a', C_b' red ROI *). In C_a and C_b, the red ROI ** is validated at –70 μm, but then is rejected by the priority rule at –60 μm (C_a', C_b' unfilled blue ROI **). A rejected neuropil is also visible at –60 μm (C_b' blue ROI).

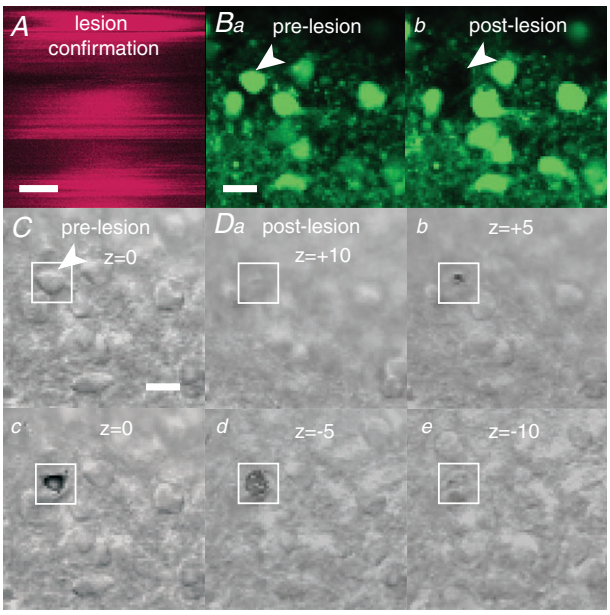

Figure 4. Laser ablation and confirmation
A, image acquired in the band 560–615 nm during maximum-intensity spot scanning for cell destruction (scale bar = 2 μm). B_{a-b}, images of Fluo-8 AM-labelled preBötC neurons before (B_a) and after (B_b) a single-cell laser ablation. The target cell (arrowhead) is visible pre-lesion but not in the post-lesion image. Neighboring (unlesioned) cells are present in both images. Scale bar = 10 μm and applies to all images in *B*–*D*. *C*, D_{a-e}, infrared-enhanced differential interference contrast images showing the target cell (white box) prior to (*C*) and after (D_{a-e}) laser lesion. Arrowhead in *C* matches *B* as a reference for target cell position. The focal plane (*C*) is normalized to $z = 0$ μm for relative comparisons with D_{a-e}, which show 5 μm increments above and below the target cell.

re-starts the lesion process, which is repeated in a loop until all the targets are exhausted (Fig. 1*B*).

We routinely detect up to hundreds of targets per experiment in the preBötC. Because laser ablation and confirmation requires 2–16 s per cell, the entire target list can be exhausted in less than 1 h. The preBötC reliably generates robust motor output at approximately 0.2 Hz in slices for many hours (Smith *et al.* 1991; Ruangkittisakul *et al.* 2006; Feldman *et al.* 2013). The straightforward result of cumulative cell-specific laser ablations is that respiratory frequency and motor output both decline, and ultimately rhythm stops altogether. This fundamental result is obtained whether cell targets are detected via Ca^{2+} imaging (Fig. 5*A*) or via fluorescent reporters (Fig. 5*B*). Cumulative single-cell ablations ostensibly disassemble the rhythmogenic core of the preBötC, which is evident by the degradation of network activity (Fig. 5; Hayes *et al.* 2012). In control experiments, where we allowed for a small movement of the slice preparation to create disparity between the map of targets and their actual locations, the rhythm was not perturbed, which suggests that indiscriminate laser pulses are not deleterious unless precisely targeted to cell somata.

Discussion

Our approach to lesioning validates cell targets according to well-defined criteria codified in Ablator software (Figs 2 and 3). The algorithms (open source Python code) can be user-modified to detect any measurable feature in a time series (obtained via Ca^{2+} imaging) or to optimize the selection of any quantifiable feature of morphology (obtained by imaging genetically encoded fluorescent proteins). Nevertheless, regardless of detection strategy, if the emitted fluorescence is insufficient, the system may overlook valid targets. Additionally, frequency is the signature feature of central pattern generator networks (Grillner, 2006; Goulding, 2009; Grillner & Jessell, 2009) and thus is useful to detect constituent neurons, but this criterion may not be appropriate for target detection in non-rhythmogenic network systems.

Calcium imaging experiments in the preBötC (e.g. Fig. 2, Supplementary Fig. 1 and Supplementary Movies 1−5) assume that rhythmic fluorescence changes reflect neuronal activity (Frermann *et al.* 1999; Koshiya & Smith, 1999; Ruangkittisakul *et al.* 2009). However, an important caveat is that rhythmicity may not always differentiate neurons from glia, as is the case in the preBötC where rhythmogenic neurons and astrocytes can oscillate with commensurate frequency (Okada *et al.* 2012), although respiratory modulated Ca^{2+} oscillations have not been universally observed in astroglia of the preBötC (Ruangkittisakul *et al.* 2009; Schnell *et al.* 2011). Although it is possible that the software may detect astrocytes in some cases rather than neurons, whole-cell recordings demonstrate that fast Ca^{2+} transients identify respiratory neurons in the majority of cases (Fig. 2*F-J*; Koshiya & Smith, 1999; Hayes *et al.* 2012).

For lesion accuracy, the present approach requires that the map of targets exactly match the physical locations of the cells. However, these two factors can become progressively uncorrelated during an experiment. A mismatch between the map of targets and the actual target positions results from mechanical lash in the translation stage, or because of tissue deformation over time. In either case, the disparity between the map and actual target locations must be rectified by stopping the ablation phase and restarting the acquisition phase (Fig. 1*B*). Minimizing the number of *xy* translations during an experiment and providing 30–60 min of 'settling in' time where the preparation resides, with perfusion, in the specimen chamber, before starting the detection phase of the experiment, can

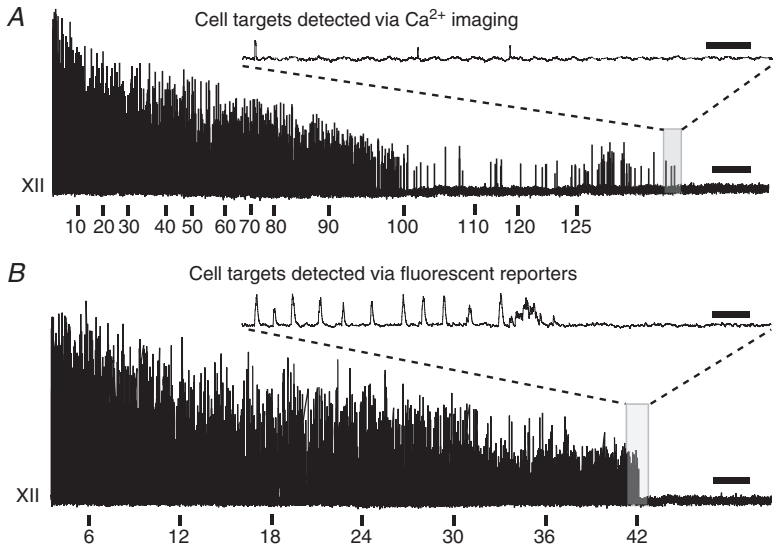

Figure 5. Cumulative cell-specific laser ablation in the preBötC
A, serial destruction of preBötC neurons detected via Ca^{2+} imaging. The abscissa is a timeline (scale bar = 5 min). The last 2 min of XII motor output are highlighted by a grey box and then expanded above (scale bar = 10 s). In the main display and the inset, the ordinate plots XII amplitude (arbitrary units). Numbered ticks (bottom) represent the tally of single-cell ablations; each lesion was confirmed according to criteria shown in Fig. 4. *B*, serial destruction of *Dbx1*$^{+}$ neurons detected via reporter expression in *Dbx1*^{LacZ} knock-in mice. Display conventions match *A* except for scale bars, which represent 2 min in the main display and 3 s in the inset (above). For *A* and *B* the recording trace is no longer displayed after 12 min of XII quiescence, although the XII output was monitored for a further 30–60 min to verify rhythm cessation.

avoid an error of this type. If the present laser ablation technique is to be adopted for use in semi-intact *in situ* preparations of the respiratory (Paton, 1996) or locomotor (Hochman *et al.* 2012) system, then a critical problem will be to minimize the mechanical disturbances caused by limb movements or cardiac pulsations that could lead to disparity of target locations and their corresponding 3D digital map.

The present method measures network output while cumulatively ablating single cells, which has been performed manually in other systems (Miller & Selverston, 1979; Bargmann & Avery, 1995; Liu & Fetcho, 1999; Eklof-Ljunggren *et al.* 2012). However, our approach is practical for mammalian models where the CNS of the organism is more opaque, cell targets are more abundant and, aside from general neuroanatomical guidelines, the specific map of targets is unknown beforehand. The most significant limitation with respect to detection and ablation pertains to laser pulses in tissue at depth. Ti:sapphire lasers can penetrate up to 900 μm in mouse tissue (Svoboda & Yasuda, 2006). However, in our experience ∼36 mW pulses (measured through the 1.0 NA objective at the specimen stage in response to 800 nm maximum intensity Ti:sapphire pulses) are rarely effective for detection and ablation deeper than 100 μm. We routinely limit the imaging and ablation depth to 80 μm because at depths exceeding 80 μm the inherent limitations can cause too many false negatives in the detection phase and in the ablation phase too many failed lesions.

The integrated instrument system we present is economically feasible. It consists of executive software (Ablator) in the public domain, which harnesses Ti:sapphire long-wavelength and visible-wavelength lasers, a laser scanning microscope and electrophysiology instruments. Two-photon confocal microscopes are accessible tools for many universities, research institutes and medical schools where neuroscience and cell biology are key research foci. Given a well-equipped core facility, the present technique can be implemented cost effectively by acquiring or fabricating a robotic translation stage. In our experience, the translation stage and digital-to-analog control circuit can be assembled for a few thousand dollars because most of the components (Supplementary Fig. 3) can be purchased off the shelf at consumer electronics stores or online. The software is customizable and free to the user. Most importantly, implementing the present technique does not irreversibly modify an existing imaging setup. If Ablator software is offline, conventional two-photon and confocal imaging applications are not affected and the robotic translation stage can be controlled manually. Therefore, single-cell laser detection and ablation experiments can be done in a shared instrument facility with no loss of function to the core instruments and without modifying the range of imaging experiments done by other users of the facility.

The technique can address the structure–function relationship of neural circuits and may provide an *in vitro* tool that complements models of neurodegenerative disease. Neurodegeneration *in vivo* takes place on various time scales from hours to weeks, months or years and may involve long-term pathological changes to cells (neurons and/or glia) and their connectivity. For example, neurodegenerative diseases can affect respiratory networks in the medulla and cause sleep-disordered breathing followed by severe respiratory pathology. One experimental model produces lesions in the rhythmogenic preBötC over several days (McKay *et al.* 2005). In contrast, the present method is limited to an abbreviated time window on the order of minutes to hours and takes place *in vitro*, and thus does not mimic slow apoptotic neurodegeneration. Therefore, the laser detection and ablation method we present may not be the ideal experimental approach in all cases. However, for modelling acute damage to the brain and CNS that could, for example, result from severe ischaemia (Lipton, 1999) or epilepsy (Meldrum, 2002), the present approach provides a useful *in vitro* model that can gauge the viability of the ensemble network as a function of the number of constituent neurons. Confining cell-specific ablations to a limited time window precludes many forms of plasticity and compensatory changes in the network structure. Therefore, the present approach could allow investigators to isolate the effects of acute cell death in simple *in vitro*, or *in situ*, disease models, which could be a useful complement to more complete *in vivo* animal models of neurodegenerative disorders.

References

Bargmann C & Avery L (1995). Laser killing of cells in *Caenorhabditis elegans*. In *Caenorbabditis elegans: modern biological analysis of an organism*, eds. Epstein, H & Shakes, D, pp. 225–250. Elsevier, Amsterdam.

Danneman PJ & Mandrell TD (1997). Evaluation of five agents/methods for anesthesia of neonatal rats. *Lab Anim Sci* **47**, 386–395.

Eklof-Ljunggren E, Haupt S, Ausborn J, Dehnisch I, Uhlen P, Higashijima S & El Manira A (2012). Origin of excitation underlying locomotion in the spinal circuit of zebrafish. *Proc Natl Acad Sci U S A* **109**, 5511–5516.

Feldman JL, Del Negro CA & Gray PA (2013). Understanding the rhythm of breathing: so near, yet so far. *Annu Rev Physiol* **75**, 423–452.

Fox J, Barthold S, Davisson M, Newcomer C, Quimby F & Smith A (eds) (2007). *Volume 3: the mouse in biomedical research, 2nd edition; normative biology, husbandry, and models*. Academic Press, Burlington, MA.

Frermann D, Keller BU & Richter DW (1999). Calcium oscillations in rhythmically active respiratory neurones in the brainstem of the mouse. *J Physiol* **515**, 119–131.

Goulding M (2009). Circuits controlling vertebrate locomotion: moving in a new direction. *Nat Rev Neurosci* **10**, 507–518.

Gray PA, Hayes JA, Ling GY, Llona I, Tupal S, Picardo MC, Ross SE, Hirata T, Corbin JG, Eugenin J & Del Negro CA (2010). Developmental origin of preBötzinger complex respiratory neurons. *J Neurosci* **30**, 14883–14895.

Grillner S (2006). Biological pattern generation: the cellular and computational logic of networks in motion. *Neuron* **52**, 751–766.

Grillner S & Jessell TM (2009). Measured motion: searching for simplicity in spinal locomotor networks. *Curr Opin Neurobiol* **19**, 572–586.

Hayes JA, Wang X & Del Negro CA (2012). Cumulative lesioning of respiratory interneurons disrupts and precludes motor rhythms in vitro. *Proc Natl Acad Sci U S A* **109**, 8286–8291.

Hirata T, Li P, Lanuza GM, Cocas LA, Huntsman MM & Corbin JG (2009). Identification of distinct telencephalic progenitor pools for neuronal diversity in the amygdala. *Nat Neurosci* **12**, 141–149.

Hochman S, Gozal EA, Hayes HB, Anderson JT, DeWeerth SP & Chang YH (2012). Enabling techniques for in vitro studies on mammalian spinal locomotor mechanisms. *Front Biosci* **17**, 2158–2180.

Koizumi H, Wilson CG, Wong S, Yamanishi T, Koshiya N & Smith JC (2008). Functional imaging, spatial reconstruction, and biophysical analysis of a respiratory motor circuit isolated in vitro. *J Neurosci* **28**, 2353–2365.

Koshiya N & Smith JC (1999). Neuronal pacemaker for breathing visualized in vitro. *Nature* **400**, 360–363.

Lipton P (1999). Ischemic cell death in brain neurons. *Physiol Rev* **79**, 1431–1568.

Liu KS & Fetcho JR (1999). Laser ablations reveal functional relationships of segmental hindbrain neurons in zebrafish. *Neuron* **23**, 325–335.

Madisen L, Zwingman TA, Sunkin SM, Oh SW, Zariwala HA, Gu H, Ng LL, Palmiter RD, Hawrylycz MJ, Jones AR, Lein ES & Zeng H (2010). A robust and high-throughput Cre reporting and characterization system for the whole mouse brain. *Nat Neurosci* **13**, 133–140.

McKay LC, Janczewski WA & Feldman JL (2005). Sleep-disordered breathing after targeted ablation of preBötzinger complex neurons. *Nat Neurosci* **8**, 1142–1144.

Meldrum BS (2002). Concept of activity-induced cell death in epilepsy: historical and contemporary perspectives. *Prog Brain Res* **135**, 3–11.

Miller JP & Selverston A (1979). Rapid killing of single neurons by irradiation of intracellularly injected dye. *Science* **206**, 702–704.

Okada Y, Sasaki T, Oku Y, Takahashi N, Seki M, Ujita S, Tanaka KF, Matsuki N & Ikegaya Y (2012). Preinspiratory calcium rise in putative pre-Bötzinger complex astrocytes. *J Physiol* **590**, 4933–4944.

Paton JF (1996). The ventral medullary respiratory network of the mature mouse studied in a working heart–brainstem preparation. *J Physiol* **493**, 819–831.

Pierani A, Moran-Rivard L, Sunshine MJ, Littman DR, Goulding M & Jessell TM (2001). Control of interneuron fate in the developing spinal cord by the progenitor homeodomain protein Dbx1. *Neuron* **29**, 367–384.

Ruangkittisakul A, Okada Y, Oku Y, Koshiya N & Ballanyi K (2009). Fluorescence imaging of active respiratory networks. *Respir Physiol Neurobiol* **168**, 26–38.

Ruangkittisakul A, Panaitescu B & Ballanyi K (2011). K^+ and Ca^{2+} dependence of inspiratory-related rhythm in novel "calibrated" mouse brainstem slices. *Respir Physiol Neurobiol* **175**, 37–48.

Ruangkittisakul A, Schwarzacher SW, Secchia L, Poon BY, Ma Y, Funk GD & Ballanyi K (2006). High sensitivity to neuromodulator-activated signaling pathways at physiological $[K^+]$ of confocally imaged respiratory center neurons in on-line-calibrated newborn rat brainstem slices. *J Neurosci* **26**, 11870–11880.

Ruangkittisakul A, Secchia L, Bornes TD, Palathinkal DM & Ballanyi K (2007). Dependence on extracellular Ca^{2+}/K^+ antagonism of inspiratory centre rhythms in slices and en bloc preparations of newborn rat brainstem. *J Physiol* **584**, 489–508.

Schnell C, Fresemann J & Hulsmann S (2011). Determinants of functional coupling between astrocytes and respiratory neurons in the pre-Bötzinger complex. *PLoS One* **6**, e26309.

Smith JC, Ellenberger HH, Ballanyi K, Richter DW & Feldman JL (1991). Pre-Bötzinger complex: a brainstem region that may generate respiratory rhythm in mammals. *Science* **254**, 726–729.

Smith JC, Greer JJ, Liu GS & Feldman JL (1990). Neural mechanisms generating respiratory pattern in mammalian brain stem-spinal cord in vitro. I. Spatiotemporal patterns of motor and medullary neuron activity. *J Neurophysiol* **64**, 1149–1169.

Svoboda K & Yasuda R (2006). Principles of two-photon excitation microscopy and its applications to neuroscience. *Neuron* **50**, 823–839.

Volgin DV, Rukhadze I & Kubin L (2008). Hypoglossal premotor neurons of the intermediate medullary reticular region express cholinergic markers. *J Appl Physiol* **105**, 1576–1584.

Author's present address

J.A. Hayes: Neurobiologie et Développement, Bâtiment 33, Avenue de la Terrasse, Institut de Neurobiologie Alfred Fessard, Centre National de la Recherche Scientifique, 91198 Gif-sur-Yvette, France, john.hayes@inaf.cnrs-gif.fr

Author contributions

J.A.H. and C.A.D.N. conceived and designed the studies. X.W., J.A.H. and M.C.P. conducted experiments. X.W. and J.A.H. devised the algorithms and analysed the data. X.W., J.A.H. and C.A.D.N. wrote the manuscript. All authors approved the final version for publication.

Acknowledgements

This work was supported by NIH grants 5 R21 NS070056-02 (PI: C.A.D.N.) and 5 R01 HL104127-03 (PI: C.A.D.N.).